JACS
JOURNAL OF THE AMERICAN CHEMICAL SOCIETY
Article
Cite This: J. Am. Chem. Soc. 2019, 141, 1606−1613
pubs.acs.org/JACS

Apoferritin Protein Amyloid Fibrils with Tunable Chirality and Polymorphism

Rocío Jurado,[†] Jozef Adamcik,[‡] Miguel López-Haro,[¶] Juan A. González-Vera,[§] Álvaro Ruiz-Arias,[§] Antoni Sánchez-Ferrer,[‡] Rafael Cuesta,[∥] José M. Domínguez-Vera,[†] José J. Calvino,[¶] Angel Orte,[§] Raffaele Mezzenga,*[,‡,⊥] and Natividad Gálvez*[,†]

[†]Department of Inorganic Chemistry, University of Granada, 18071 Granada, Spain
[‡]Department of Health Sciences and Technology, ETH Zürich, 8092 Zürich, Switzerland
[¶]Department of Material Science and Metallurgy Engineering and Inorganic Chemistry, University of Cádiz, 11510, Cádiz, Spain
[§]Department of Physical Chemistry, Faculty of Pharmacy, University of Granada, Campus Cartuja, 18071, Granada, Spain
[∥]Department of Organic and Inorganic Chemistry, EPS Linares, University of Jaén, 23700 Linares, Spain
[⊥]Department of Materials, ETH Zürich, 8093 Zürich, Switzerland

Supporting Information

ABSTRACT: Ferritin, a soluble and highly robust protein with subunits packed into well-defined helices, is a key component of the iron regulatory system in the brain and thus is widely recognized as a crucial protein for iron metabolism, but may also bear possible implications in some neurodegenerative disorders. Here, we present evidence of how human recombinant apoferritin can convert into an unusual structure from its folded native state; that is, amyloid fibrils analogue to those found in pathological disorders such as Alzheimer's and Parkinson's diseases. An extensive combination of advanced microscopy, spectroscopy and scattering techniques concur to reveal that apoferritin fibrils possess a common double stranded twisted ribbon structure which can result in a mesoscopic right-handed chirality. We highlight a direct connection between the chirality and morphology of the resulting amyloid fibrils, and the initial protein subunits composition, advancing our understanding on the possible role of misfolding in some ferritin-related pathologies and posing new bases for the design of chiral 1D functional nanostructures.

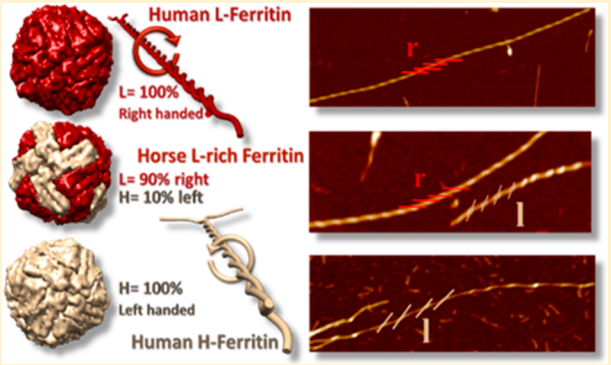

INTRODUCTION

The extraordinary and common ferritin protein has an essential metabolic role involving iron storage and homeostasis for practically all life forms.[1] The universal ferritin protein family is characterized by a remarkable conservation of its unique three-dimensional architecture designed to uptake iron, in a soluble, bioavailable and safe form, not only to protect cells against iron-mediated radical chemistry but also to regulate its availability under conditions of cellular iron demand.[2]

The genuine apoferritin (APO), the iron-free ferritin molecule, is a hollow globular protein composed of 24 polypeptide subunits (M_n ∼ 480 kDa) where Fe(III) is accommodated as an iron oxyhydroxide nanoparticle.[3] In eukaryotes, APO organic shell is the product of the self-assembly of mainly two primary peptide subunits or chains: L "light" (∼20 kDa), and H "heavy" (∼21 kDa). Indeed, Arosio and colleagues nicely reported that each subunit has been assigned to a specific role: H-chains display ferroxidase activity able to catalyze the oxidation of Fe(II) to Fe(III), while L-chains have nucleation sites for iron oxyhydroxides formation.[2,4,5] The assembly of the H- and L-subunits into the 24-mer APO capsid produces a variety of different ferritin molecules (isoferritins) whose H/L ratio is genetically controlled in each tissue (Figure 1). Thus, tissues with iron storage function (liver and spleen) contain L-rich (up to 90% of L-subunits) ferritins, that may accommodate high iron amounts, whereas in detox activity tissues (heart and brain) the number of H-subunits increases (up to 50% of H-subunits), with the aim to catalytically oxidize Fe(II) to Fe(III), thus avoiding the formation of reactive-oxygen species. Any disruption of the ferritin H/L ratio or a mutation in the H- or L-subunit is related in fact, to the origin of a pathology.[6,7] As an example, ferritin expression level and amount of Fe(III) stored have been reported to be altered in diseases such as Parkinson's, Alzheimer's[8] or acquired immunodeficiency syndrome (AIDS).[1,9] In addition, it has been recently reported

Received: October 23, 2018
Published: December 27, 2018

DOI: 10.1021/jacs.8b11418
J. Am. Chem. Soc. 2019, 141, 1606−1613

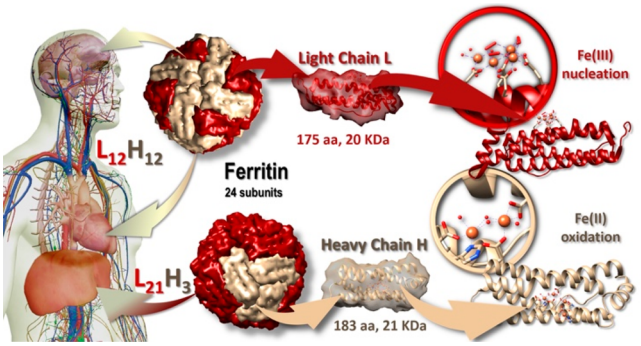

Figure 1. Subunit composition for different human isoferritins. Human L-chains are represented in red and human H-chains in gray. The average subunit composition for liver ($L_{21}H_3$) and brain ($L_{12}H_{12}$) ferritins are shown. The ferroxidase center buried inside the α-helix bundle of the ferritin H-chain as well as the nucleation center for ferritin L-chain are also displayed.

that the prevalence of iron in breast cancer cells points toward iron and iron-mediated processes as potential targets against these cells.[10]

Amyloid fibrils are usually related to human diseases, including numerous neurodegenerative disorders.[11−14] However, natural amyloid fibrils formed under nonpathological conditions have functional roles in living systems.[15−17] Furthermore, amyloid fibrils as well as ferritin proteins have properties that have potential significance for the development of new artificial nanohybrid materials, as undoubtedly advanced by Gazit and Reches for peptides or Böker et al. in the case of ferritin.[18−21]

Morphological heterogeneity in amyloid fibrils, such as twisted ribbons, helical ribbons, or nanotubes-like structures is generally referred as structural polymorphism of amyloid fibrils.[22] Amyloid polymorphism is also demonstrated in their superstructure chirality. For example, it has been previously demonstrated that the spontaneous inversion of chirality can be caused by small changes in the experimental conditions used to form the fibrils.[23,24] Understanding the 3D structure and chirality of polypeptide fibril superstructure is a key issue because they are linked to its biochemical activity and associated toxicity,[25−27] and because once controlled, it could be tuned to access novel synthetic protein-based nanomaterials.[28]

Recently, we have reported that the globular horse spleen apoferritin protein (L-rich APO= $L_{21}H_3$) can undergo a fibrillization process, forming fibrils from temperatures ranging from 50 °C (close to physiological conditions) to 80 °C and pHs varying from 2 to 5.[29] Here, we confirm the amyloid nature of these fibrils, and we present first, that human APO also forms amyloid fibrils and second, that the primary H- and L-APO chains, which have a matched peptide sequence of only 54−57%,[2] drive the final chirality and polymorphism. We compare the horse spleen L-rich APO amyloid fibrils, with amyloid fibrils formed from human recombinant H-APO (H-APO= H_{24}) and from human recombinant L-APO (L-APO= L_{24}). Single-molecule atomic force microscopy (AFM) and high-resolution electron tomography in the high angle annular dark field scanning transmission electron microscopy mode (HAADF-STEM) have been used to investigate the structural morphology of assembled APO amyloid fibrils. Additionally, the APO fibrillization kinetic process has been followed by advanced fluorescence lifetime imaging microscopy with pulsed interleaved excitation scheme (FLIM-PIE). The results we present here are striking because, while amyloid fibrils from human APO have not been reported before, this protein is increasingly being recognized as a crucial molecule in some neurological pathologies.[4] All combined experiments point at the peptide sequence of the APO protein as a main determinant controlling the fibril final morphology and chirality. As chiral information is embedded in the amyloid structure, controlling the chirality could allow fine-tuning of nanostructure functions.

RESULTS AND DISCUSSION

L-rich APO protein forms fibrillar structures (Figure S1a,d) similar to other globular proteins when subjected to denaturing conditions, specifically in this work, 9 h of protein incubation at pH 2 and 90 °C.[28,30] The L-rich APO fibrils morphology was characterized in detail using AFM, which revealed details of the structure at the single fibril length scale. Surprisingly, the L-rich APO fibrils possess morphology of twisted ribbons with two types of chirality, thus a coexistence of right- and left-handed fibrils was observed (Figures 2a, S1d and S3a). Usually, amyloid fibrils assembled from native globular proteins under appropriate fibrillization conditions are left-handed. This right-handed fibril chirality shown by L-rich APO protein has not been previously observed for native globular proteins. Inversion on handedness from left to right with processing conditions or with incubation time has been reported for insulin and albumin but right-handed amyloid fibrils have only been described for amyloid-forming small peptides.[23,24,31−33]

In addition, around 87% of L-rich APO fibrils were right-handed, around 6% were left-handed and around 7% possess nanotube-like structure (Figure 2l). Taking into account that the L/H composition in L-rich APO has a 90:10 wt % ratio ($L_{21}H_3$), one can expect that the subunit peptide sequence may be at the origin of the observed different chirality. Therefore, using the same experimental conditions (see methods), we prepared fibrils starting from both, pure human L-APO and H-APO. In the case of both human APOs the formation of amyloid fibrils similar to L-rich APO was observed (Figures S1b, S1c, S3b and S3c). Interestingly, the observed chirality was mainly right-handed for the L-APO fibrils and left-handed for the H-APO fibrils (Figures 2e, 2i, S1e,f and S3). Specifically, 95% of fibrils were right-handed for L-APO and 93% of fibrils were left-handed for H-APO (Figure 2l).

In order to characterize all three classes of assembled APO amyloid fibrils in more detail, a statistical analysis of AFM images was performed[34] and the morphological parameters such as pitch size, average height and contour length were evaluated (Figures 2 and S2).

The pitch size estimation of amyloid fibrils was calculated from the autocorrelation function (ACF) of AFM images (Figure 2b,f,j) and from the discrete Fourier transform (DFT) of AFM images (Figure 2c,g,k). The right-handed L-rich APO and L-APO fibrils have periodicities around 47 and 46 nm, respectively. In the case of left-landed L-rich APO and H-APO fibrils, the periodicity was around 101 and 82 nm, respectively.

All three classes of APO fibrils are several micrometres long semiflexible fibrils (Figure 2d), thus the contour length does not seem to be a key factor when distinguishing fibrils, because its value varies between 1 and 8 μm for all cases.

Significant difference between APO fibrils was observed in their height. Left-handed H-APO fibrils with average height of 3.6 nm are thinner in comparison with right-handed L-APO or L-rich APO fibrils with average height around 7.0 nm (Figure 2h).

DOI: 10.1021/jacs.8b11418
J. Am. Chem. Soc. 2019, 141, 1606−1613

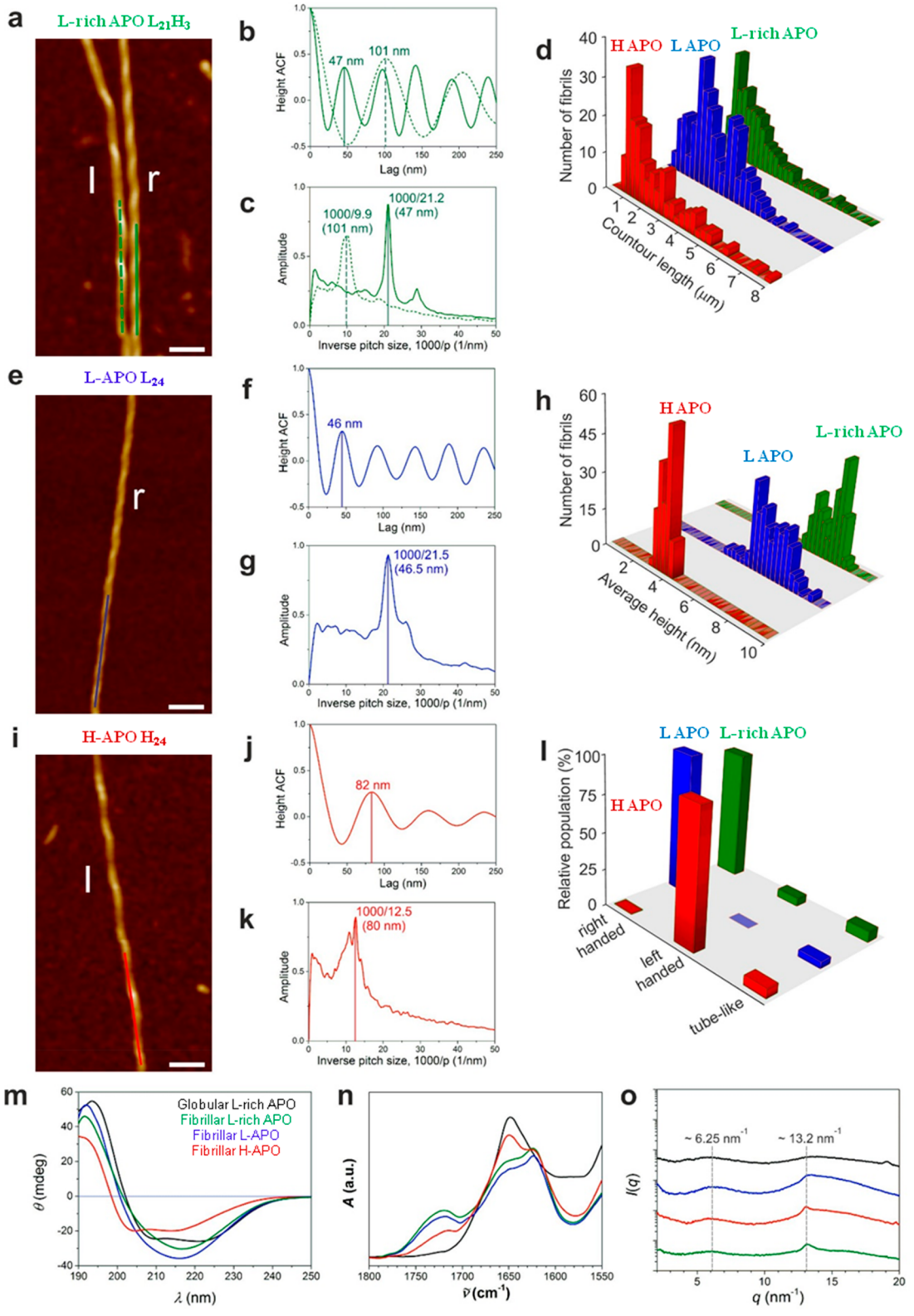

Figure 2. AFM image of (a) r: right-handed and l: left-handed L-rich APO; (e) r: right handed L-APO and (i) l: left-handed H-APO fibrils. Scale bars represent 50 nm. Estimation of the pitch calculated from the autocorrelation function (ACF) of AFM images of (b) L-rich APO (green color; dashed line corresponds to l: left-handed fibrils, solid line corresponds to r: right-handed fibrils), (f) L-APO (blue color) and (j) H-APO (red color). Estimation of the pitch calculated from the discrete Fourier transform (DFT) of AFM images of (c) L-rich APO, (g) L-APO and (k) H-APO. (d) Contour length distribution and (h) average height distribution of amyloid fibrils. (l) Relative population of right handed, left handed and tube-like fibrils. (m) CD spectra, (n) FTIR spectra and (o) WAXS intensity profiles of amyloid fibrils and globular L-rich APO (black color).

The persistence length (L_p) of APO fibrils was also extracted from the statistical analysis (Figure S2a,bc) showing that right-handed fibrils have slightly higher persistence length compared to left-handed fibrils.[30,31] To estimate mechanical properties of

DOI: 10.1021/jacs.8b11418
J. Am. Chem. Soc. 2019, 141, 1606−1613

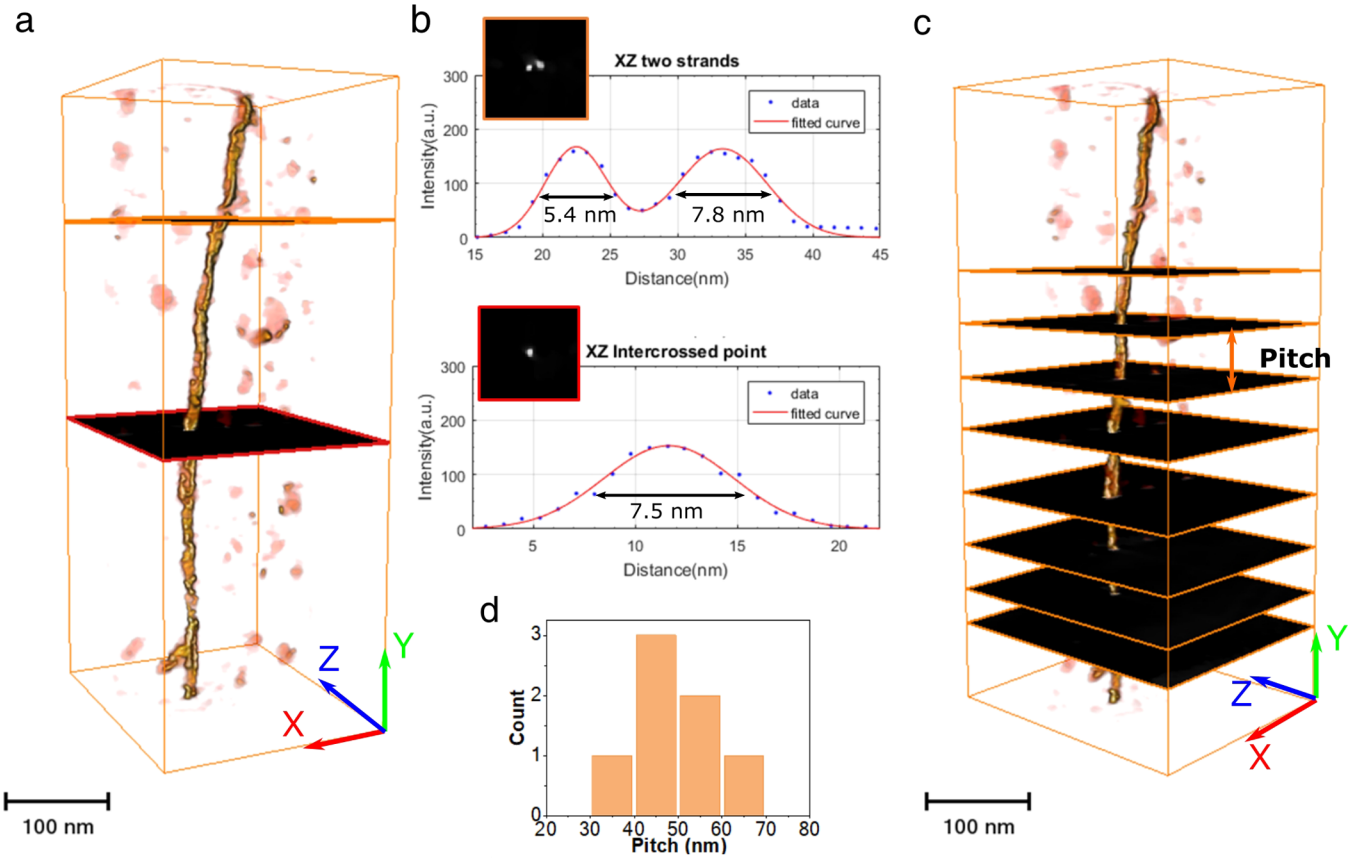

Figure 3. HAADF-STEM tomography study of horse L-rich APO fibrils. (a) 3D volume rendering of a L-rich APO fibril; (b) XZ orthoslices extracted from the reconstructed volume at the locations marked on panel a, and intensity profiles along lines crossing the dot features - top and middle figures; histogram of pitch values—bottom figure; (c) a sketch illustrating the procedure used to determine the pitch values along the fibrils. The planes included in the sketch locate the positions of the fibril where the XZ orthoslices show only one spot, i.e., the locations along the fibril of minimum apparent width distance.

L-rich APO fibrils, the Young's modulus was measured using AFM nanoindentation showing that its value (Figure S2d,e) is in the range of GPa typical for amyloid fibrils.[35]

Knowing that L- and H-subunits drive the final chirality and polymorphism of the APO fibrils, we further investigated possible variations in their secondary structure. The hallmark of amyloid assemblies is a conformational transition of the constituent monomeric proteins into a β-sheet rich fibril.[12] Circular dichroism (CD) (Figures 2m and S4) gave evidence of slight differences between the secondary structure of the right-handed L-APO and left-handed H-APO fibrils. In general, upon fibrillization, the APO protein loses α-helix content and gains β-sheet structure, supporting a pathway toward an amyloid fibrillization. Fourier transform infrared spectroscopy (FTIR) results (Figures 2n and S5) further confirm that the two types of fibrils have a structure that differs from the native globular conformation and that the cross-β region, characteristic of amyloid structures, become predominant in APO fibrils.

The wide-angle X-ray scattering (WAXS) profile from APO amyloid fibrils shows the characteristic peaks centered at q = 6.3 and 13.2 nm^{-1}, which correspond to the β-sheet ($d_{\beta\text{-sheet}}$ = 1.0 nm) and β-strand ($d_{\beta\text{-strand}}$ = 4.8 Å) distances, respectively (Figures 2o and S6–S9). In contrast, globular native APO rather shows a random pattern, with no sharp peaks, but a broad distribution in agreement with the CD and FTIR results.

Gel electrophoresis (SDS-PAGE) and mass spectrometry (MALDI-MS) were used to get a better understanding of how the L/H APO composition, that is the subunit peptides, may be at the origin of the observed different chirality and polymorphism.

The SDS-PAGE results (Figure S10) confirmed the decisive role of protein hydrolysis in the formation of amyloid fibrils. Indeed, hydrolyzed L-rich APO peptide fragments are already present in solution after 30 min of heat treatment. Similar results were obtained from H-APO and L-APO fibrils.

We intended to determine, by MALDI-MS, the exact amino acid (AA) sequences that are involved in the different APO fibrils. In the case of human L-APO the two main peaks correspond to the same sequence Asp95-Pro124 with only one Proline residue difference for m/z = 2865 Da (Figure S11), which corresponds to 27–28 amino acids with a fully stretched peptide length of ca.10 nm. Interestingly, these peptide fragments did not appear for the human H-APO fibrils (Figure S12), where the main peaks correspond to the sequence Met1-Gln15 and His152-Phe171 with m/z = 1781 and 2233 Da, respectively. These two main sequences contain 15 and 20 amino acids, and the fully stretched peptide length spans from 5 to 7 nm. In the case of horse L-rich APO fibrils (Figure S13), two peaks corresponding to the same sequence Ser17-Phe42 with one Aspartic acid residue difference for m/z = 3066 Da, which correspond to 26–27 amino acids with a fully stretched peptide length of ca.10 nm, are identified and confirmed by MS/MS. Thus, we can tentatively infer that the two main polymorphs, right- and left-handed fibrils, are built from different APO

DOI: 10.1021/jacs.8b11418
J. Am. Chem. Soc. 2019, 141, 1606–1613

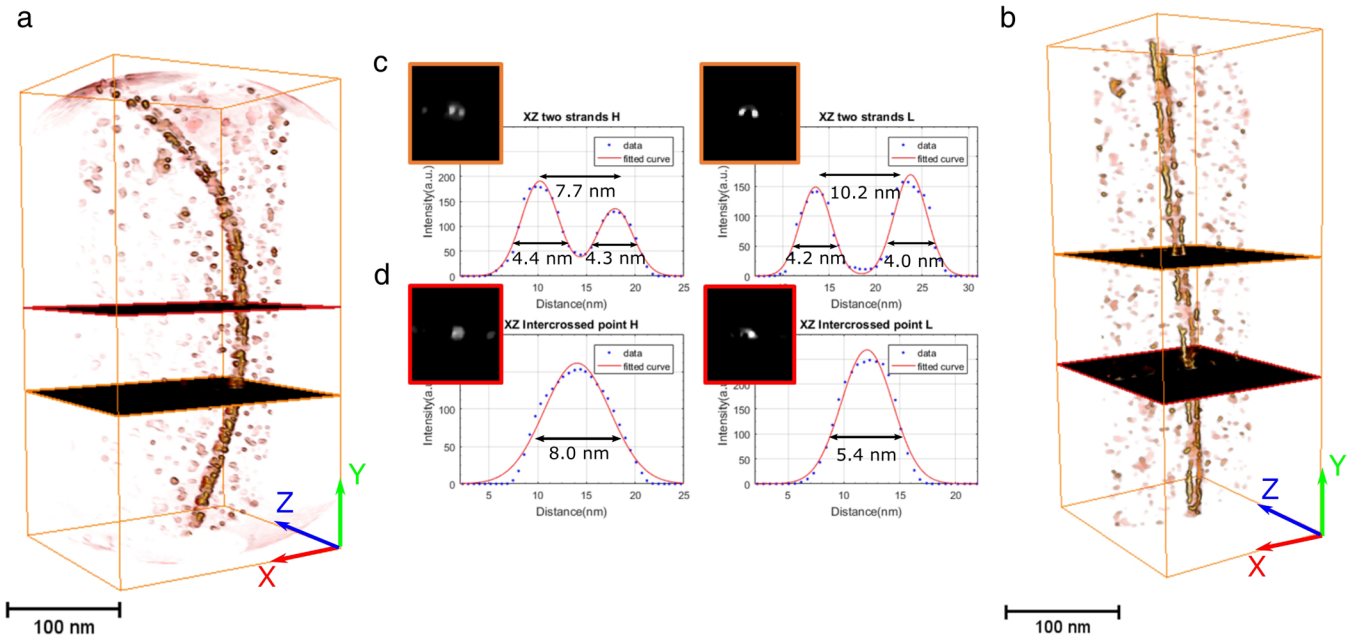

Figure 4. HAADF-STEM tomography study of H-APO and L-APO fibrils. (a) 3D volume rendering of a H- APO fibril; (b) 3D volume rendering of a L- APO fibril; (c and d) XZ orthoslices at the locations marked in panels a and b. The intensity profiles are also included. In the images shown at the top row, two strands are observed both in the L- and H-APO fibrils whereas the orthoslices at the bottom correspond to the location of minimum apparent width distance.

peptide fragments, and that apparently these primary peptide subunits control the final tertiary and quaternary structure. Similarly, in all the three classes, the length of the fully extended main peptidic blocks is 1.4 to 2 times the height of the fibrils, which infers that the peptide is folded at least once within each protofilament, in a hairpin-like fold.

To further investigate the morphology and to unveil the 3D organization at nanometric scale of APO fibrils, high-resolution HAADF-STEM electron tomography (ET) experiments were performed. ET has proven to be a powerful tool for obtaining detailed 3D structures and therefore for the characterization of macro-molecular assemblies and different nanostructures at very high resolution.[36−41] In a first step, ET analysis was performed in HAADF-STEM mode for the L-rich APO fibrils. The 3D volume rendering of the reconstruction of an isolated L-rich APO fibril (Figure 3a) shows its twisted structure. Interestingly, the ET reconstruction reveals that this fibril contains a pair of intertwined protofilaments (Figure 3a), as confirmed in TEM (Figure S14). This can be better observed in the orthoslices perpendicular to the fibril axis (XZ planes marked in Figure 3a). Note that at some locations along the fibril, as that corresponding to the upper plane in Figure 3a, two white spots are clearly observed (top image in Figure 3b), each one corresponding to the cross-section of one protofilament. At specific locations along the fibril, only one spot is observed in the orthoslices in a way that the width of these fibrils would seem to vary periodically between roughly 15 nm (Figure 3b) and 7.5 nm (Figure 3b bottom). However, STEM-HAADF ET images were obtained with conventional negative staining and it is important to realize that contrast in the negatively stained images arises primarily from the uranyl acetate stain, not from the fibrils themselves. Indeed, as expected, no width modulation is observed in unstained AFM images, in line with the constant distance among protofilaments in other classes of double-stranded amyloid twisted ribbons.[30] Accumulation of stain around areas of contact between fibrils and the carbon film on the TEM grid produces an amplification of the apparent width modulation (Figure S14).[42] Interestingly, by measuring the distance between neighboring locations along the fibril depicting minimum apparent width distance, as sketched in Figure 3c, it has been possible to estimate the pitch of the repeating twisted superstructure from the STEM-HAADF ET experiments. The distribution of pitch values measured using this procedure (Figure 3c,d) spans from 35 to 65 nm, with an average value near to 50 nm close to that obtained from AFM (Figure 2b,c). The maximum apparent width distance determined as roughly 15 nm is in good agreement with width measured by conventional TEM (Figure S14).

The details of the nanometric-level structure of these twisted fibrils are difficult to discern by TEM images, which are just two-dimensional density projections. However, the double stranded structure, as well as the twisted nature of the paired fibrils, is definitely revealed when the assembly is resolved by 3D tomography and AFM images.

H-APO and L-APO fibrils were additionally analyzed by ET (Figure 4). Figure 4a,b represents the 3D rendering of the reconstructed volume of single H- and L-APO fibrils, respectively. The maximum apparent width distance values are similar for both samples, 13 nm for H-APO and 12.5 nm for L-APO, and similar to L-rich APO (Figure S14). Measuring locations along the fibril depicting minimum apparent width distance clear differences were observed in the pitch values, with an average value of 57 nm for the L-APO and 93 nm for the H-APO fibril. We have to highlight that the mean pitch values obtained by 3D reconstruction from ET studies are in excellent agreement with the periodicity values obtained from AFM statistical analysis (Figure 2).

Neither the hierarchical assembly of paired strands into APO fibrils has been previously described, nor the formation of amyloid fibrils for L- and H- recombinant human APO protein. Our three-dimensional analysis strongly suggests that all APO fibrils have a common building block comprising paired

DOI: 10.1021/jacs.8b11418
J. Am. Chem. Soc. 2019, 141, 1606−1613

protofilaments with a twisted substructure. Both techniques, AFM image analysis and high-resolution ET, hence proved to be of great value for obtaining complementary information about the morphology, superstructure and handedness of APO amyloid fibrils.

To obtain additional information on the nature of the oligomers formed in the early stages of the APO fibrillization process and their time evolution, we explored the use of single-molecule resolution fluorescence microscopy, as a powerful tool to monitor assembly processes.[43−45] To study these aggregates, we employed an advanced fluorescence lifetime imaging microscopy with pulsed interleaved excitation scheme (FLIM-PIE). The FLIM microscopy presents many advantages compared to conventional fluorescence microscopy, especially for quantitative measurements (SI and S15).[46] Using this technique, we studied the kinetics of L-rich APO aggregation at different incubation times (Figures 5a and S16). The incubation

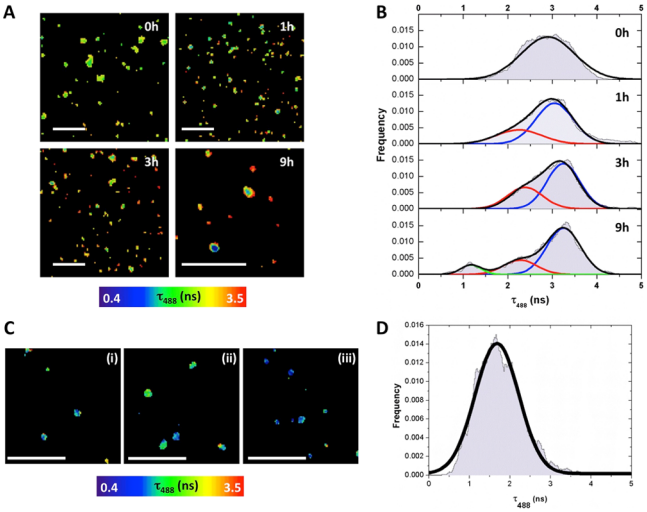

Figure 5. (a) Representative donor (A488) FLIM images of L-rich APO aggregates after different incubation times. (b) Frequency histograms of τ_{A488} values in L-rich APO aggregates, averaged for at least 10 different images. (c) Representative donor FLIM images of insoluble aggregates found in filtered samples of L-rich APO incubated for 9 h. (d) Corresponding frequency histogram of τ_{A488} values in insoluble L-rich APO aggregates described in panel c, averaged over 10 different images. Scale bars represent 5 μm.

of equimolar mixtures of donor- and acceptor-labeled L-rich APO subunits under fibril formation conditions (pH 2, 90 °C) for several hours resulted in the effective coaggregation and formation of mature fibrils. The presence of the dye molecules does not alter the fundamental features and kinetics of the aggregation reaction or the appearance of the resulting fibrillar aggregates (Figures S17 and S18). When focusing on the aggregates formed in the early stages, the distribution of FRET values significantly varied with the size of the oligomers (Figure 5b), revealing three dominant populations, a low-FRET population with $\tau_{A488} > 3$ ns ($E < 0.27$); a mid-FRET population with $\tau_{A488} = 2.2$ ns ($E = 0.46$); and a high-FRET population with $\tau_{A488} = 1.1$ ns ($E = 0.73$). The mid-FRET population appeared after 1 h of incubation, whereas the high-FRET aggregates arose after 9 h of incubation time. Of particular importance in this study has been the identification of a slow conversion from the initially formed and readily degradable oligomers to compact and highly structured oligomers in concordance with an increase in the amyloid-like β-sheet structures.

Interestingly, when the 9 h-incubated solution was filtered, and the remaining aggregates were imaged the single remaining population was that of high-FRET (Figure 5c), exhibiting an average $\tau_{A488} = 1.6$ ns ($E = 0.61$, Figure 5d). This result confirms that the low-FRET and most of the mid-FRET aggregates are still soluble. However, the detected population likely contains certain contribution of mid-FRET aggregates, so that the average distribution is broader and shifted to slightly larger τ_{A488} values.

The presence of aggregates with different compactness, and therefore FRET efficiency, is in line with the heterogeneous nature of the amyloid fibrillization and the formation of fibrils with polymorphism in the final structures. Similar results were obtained for human L- and H-APO fibrils (Figures S19−S22), evidencing, however, slight differences in the aggregation pathway (see SI for details) that may be behind the chirality selection of fibril formation.

CONCLUSIONS

We have discovered that ferritin, a key component of the iron regulatory system in the brain, can convert into amyloid fibrils with polymorphism sharing common traits with pathological amyloid fibrils found in Alzheimer's and Parkinson's diseases. The formation of amyloid fibrils from both L- and H-recombinant human APO protein was followed and resolved from the early aggregation stages to their final hierarchical assembly into double-stranded twisted ribbons. Interestingly it was shown that native APO proteins can form fibrils with both a left- (when starting from pure L-APO) and right-handed chirality (when starting from pure H-APO), and resolution of their molecular composition from MALDI points directly to a peptide sequence-controlled determinant for chiral selectivity.

These results open up the possibility of using polypeptide chain primary structure as a mean to access new forms of protein tertiary and quaternary nanostructures and highlight how the peptide sequence of such structures can tune the macroscopic chirality. Because chiral information is embedded in the helical structure, selecting a specific handedness a-priori could allow dynamic control of nanostructure functions and pose new bases for the design of chiral filaments and 1D nanostructures.

EXPERIMENTAL SECTION

Preparation of Horse Spleen L-Rich APO Fibrils and Human L- and H-APO Fibrils. Horse spleen APO protein was purchased from Sigma-Aldrich and was used without further manipulation. Human L- and H-APO proteins were purchased from MoLiRom and purified by dialyzing for 24 h against several changes of Milli-Q water. Purified protein solutions (0.1 wt %) were adjusted to pH 2 (diluted HCl dissolved in Milli-Q water) before heat treatment (90 °C, glass tubes hermetically sealed) over incubation timeperiod of 9 h and under magnetic agitation (90 rpm). After heat treatment, glass tubes were cooled in an ice bath to quench the aggregation process and stored at 4 °C. Samples were collected for TEM and AFM analysis.

Preparation of the Dye-Labeled L-Rich APO Fibril Proteins. Atto succinimidyl ester derivatives of the donor, Atto 488 (A488), and the acceptor, Atto647N (A647), fluorophores were purchased from Atto-Tec GmbH. The Förster distance, R_0, for this pair of fluorophores is 51 Å, which allowed us to detect the formation of aggregates at the single-molecule level based on the FRET efficiency, E, when the labeled monomers interacted with each other. Solutions of globular horse spleen apoferritin protein, human L-APO, or human H-APO (0.1 wt %, 2 mL) were prepared in aqueous solution at pH 8.0 and incubated for 1 h with the corresponding fluorophore succinimidyl ester derivatives.

DOI: 10.1021/jacs.8b11418
J. Am. Chem. Soc. 2019, 141, 1606−1613

The resulting solutions were then exhaustively dialyzed for 2 days against several changes of distilled water. The samples were collected and mixed in a 1/1 (A488-protein:A647-protein) stoichiometry. Subsequently, samples were adjusted to the appropriate pH 2 (diluted HCl dissolved in Milli-Q water) before heat treatment (90 °C, glass tubes hermetically sealed) at different times (1, 3 and 9 h) and quenched immediately in a water−ice bath. An aliquot of the sample heated for 9 h was centrifuged 3 times using Amicon Ultra-4 centrifugal filter devices with a molecular weight cutoff (MWCO) of 50 000 Da and the supernatant was recovered. All samples were characterized by fluorescence spectroscopy (Varian Cary Eclipse Fluorescence Spectrophotometer). Samples for TEM and AFM were prepared following the same methods as mentioned before. Samples for gel electrophoresis were prepared following the same previous method but a concentration of 0.05 wt % of protein was used for all aliquots.

Samples for Atomic Force Microscopy (AFM). AFM experiments were carried out on a Multimode 8 Scanning Force Microscope (Bruker, USA) covered with an acoustic hood to minimize vibrational noise. A droplet of solution of different samples (0.1 wt %) was deposited onto freshly cleaved mica, incubated for 2 min, rinsed with Milli-Q water and dried by nitrogen. The AFM was operated in tapping mode under ambient conditions using commercial silicon nitride cantilevers (Bruker, USA) at a vibrating frequency of 150 kHz. Images were simply flattened using the Nanoscope 8.1 software, and no further image processing was carried out. The images acquired were used for the statistical analysis using the open source software FiberApp.[34] We analyze a total of 446 fibers adding for L-rich APO (181), L-APO (81) and H-APO (184).

Electron Tomography (ET). Experiments were performed in a FEI Titan Themis 60-300 Double Aberration Corrected microscope operated at 80 kV. A convergence angle of 9 mrad was selected in order to improve the depth of focus. In particular, a camera length of 115 mm was used. Then, a series of STEM-HAADF images at different tilts were recorded using the software FEI Explore3D v.4.1. The tracking, focusing and tilting were carried out automatically. The samples were tilted from −70° to +70° and images acquired every 5°. To denoise the tilt series, homemade scripts in MATLAB were made using the WAVELAB850 toolbox (http://statweb.stanford.edu/~wavelab/Wavelab_850/index_wavelab850.html) and the *invansc* package, downloaded from http://www.cs.tut.fi/~foi/invansc. In fact, denoising was performed using a combination of the Anscomb and Wavelet Transforms. The whole set of HAADF-STEM denoised images were aligned combining a cross-correlation method, using FEI Inspect3D v 4.1, and the landmark-based alignment implemented in TomoJ. The tilt series images were also background-subtracted, normalized and binned to 512 × 512 pixels. Afterward, images were reconstructed into a 3D volume using a Compressed Sensing algorithm based on Minimization of the Total Variation (TVM) of each single STEM-HAADF image. In particular, a 3D implementation of the TVAL3 routine, using AstraToolBox, was employed. For visualization and further nanometrological analysis of the reconstructed volumes, the FEI Avizo 7.0 software was used.

Fluorescence Lifetime Imaging Microscopy with Pulsed Interleaved Excitation (FLIM-PIE) Measurements. FLIM-PIE experiments of dye-labeled human H-APO, human L-APO, and horse L-rich APO fibrils were performed with a MicroTime 200 time-resolved fluorescence microscope (Pico-Quant GmbH, Germany).[29] We employed a dual-color pulsed interleaved excitation (PIE) scheme, with two spatially overlapped pulsed lasers, at 470 (LDH-P-C-470, PicoQuant) and 635 nm (LDH-P-635, PicoQuant).

These settings permit the simultaneous collection in a single step of the donor FLIM image, the FRET image, and the directly excited acceptor fluorescence intensity image. The images were collected by raster-scanning different areas, using a 512 × 512 pixel resolution, and a 60 ms/pixel acquisition time. The FLIM analysis of the donor images was carried out in SymPhoTime 32 (PicoQuant) by fitting the fluorescence decay traces obtained in the individual pixels to a single exponential decay function after a 5 × 5 spatial binning, using the maximum likelihood estimator (MLE) for parameter optimization. Selection of pixels corresponding to aggregates (Figure S15) was performed using home-coded scripts in FiJi (distribution of ImageJ2).[47]

■ ASSOCIATED CONTENT

Supporting Information

The Supporting Information is available free of charge on the ACS Publications website at DOI: 10.1021/jacs.8b11418.

Full experimental methods; additional characterizations presented: TEM images, AFM images and structural characterization of APO fibrils; CD spectra, FTIR spectra, WAXS scattering profile, SDS-PAGE electrophoresis and MS spectra for APO fibrils; FLIM-PIE imaging of APO aggregates; TEM images, AFM images and SDS-PAGE electrophoresis of functionalized L-rich APO fibrils; additional FLIM-PIE results on functionalized human L-APO and H-APO aggregates (PDF)

■ AUTHOR INFORMATION

Corresponding Authors

*ngalvez@ugr.es

*raffaele.mezzenga@hest.ethz.ch

ORCID

Miguel López-Haro: 0000-0003-2560-8015

Antoni Sánchez-Ferrer: 0000-0002-1041-0324

José J. Calvino: 0000-0002-0989-1335

Angel Orte: 0000-0003-1905-4183

Raffaele Mezzenga: 0000-0002-5739-2610

Natividad Gálvez: 0000-0003-4286-6278

Notes

The authors declare no competing financial interest.

■ ACKNOWLEDGMENTS

R.J. thanks the Boehringer Ingelheim Fonds for a travel grant. This work was funded by the Junta de Andalucía Project P11-FQM-8136 and MINECO Project CTQ2015-64538. The authors acknowledge the "Unidad de Excelencia de Química aplicada a Biomedicina y Medioambiente", Universidad de Granada.

■ REFERENCES

(1) Honarmand Ebrahimi, K.; Hagedoorn, P. L.; Hagen, W. R. Unity in the Biochemistry of the Iron-Storage Proteins Ferritin and Bacterioferritin. *Chem. Rev.* **2015**, *115*, 295−326.

(2) Harrison, P. M.; Arosio, P. The Ferritins: Molecular Properties, Iron Storage Function and Cellular Regulation. *Biochim. Biophys. Acta, Bioenerg.* **1996**, *1275*, 161−203.

(3) Chasteen, N. D.; Harrison, P. M. Mineralization in Ferritin: An Efficient Means of Iron Storage. *J. Struct. Biol.* **1999**, *126*, 182−194.

(4) Finazzi, D.; Arosio, P. Biology of Ferritin in Mammals: An Update on Iron Storage, Oxidative Damage and Neurodegeneration. *Arch. Toxicol.* **2014**, *88*, 1787−1802.

(5) Lawson, D. M.; Artymiuk, P. J.; Yewdall, S. J.; Smith, J. M. A.; Livingstone, J. C.; Treffry, A.; Luzzago, A.; Levi, S.; Arosio, P.; Cesareni, G.; et al. Solving the Structure of Human H Ferritin by Genetically Engineering Intermolecular Crystal Contacts. *Nature* **1991**, *349*, 541−544.

(6) Ferreira, C.; Bucchini, D.; Martin, M.; Levi, S.; Arosio, P.; Grandchamp, B.; Beaumont, C. Early Embryonic Lethality of H Ferritin Early Embryonic Lethality of H Ferritin Gene Deletion in Mice. *J. Biol. Chem.* **2000**, *275*, 3021−3024.

(7) Curtis, A. R.; Fey, C.; Morris, C. M.; Bindoff, L. A.; Ince, P. G.; Chinnery, P. F.; Coulthard, A.; Jackson, M. J.; Jackson, A. P.; McHale, D. P.; et al. Mutation in the Gene Encoding Ferritin Light Polypeptide

DOI: 10.1021/jacs.8b11418
J. Am. Chem. Soc. 2019, 141, 1606−1613

Causes Dominant Adult-Onset Basal Ganglia Disease. *Nat. Genet.* **2001**, *28*, 350−354.
(8) Connor, J. R.; Snyder, B. S.; Arosio, P.; Loeffler, D. A.; LeWitt, P. A Quantitative Analysis of Isoferritins in Select Regions of Aged, Parkinsonian, and Alzheimer's Diseased Brains. *J. Neurochem.* **1995**, *65*, 717−724.
(9) Drakesmith, H.; Chen, N.; Ledermann, H.; Screaton, G.; Townsend, A.; Xu, X.-N. HIV-1 Nef down-Regulates the Hemochromatosis Protein HFE, Manipulating Cellular Iron Homeostasis. *Proc. Natl. Acad. Sci. U. S. A.* **2005**, *102*, 11017−11022.
(10) Mai, T. T.; Hamaï, A.; Hienzsch, A.; Cañeque, T.; Müller, S.; Wicinski, J.; Cabaud, O.; Leroy, C.; David, A.; Acevedo, V.; et al. Salinomycin Kills Cancer Stem Cells by Sequestering Iron in Lysosomes. *Nat. Chem.* **2017**, *9*, 1025−1033.
(11) Dobson, C. M. Protein Folding and Misfolding. *Nature* **2003**, *426*, 884−890.
(12) Chiti, F.; Dobson, C. M. Protein Misfolding, Amyloid Formation, and Human Disease: A Summary of Progress Over the Last Decade. *Annu. Rev. Biochem.* **2017**, *86*, 27−68.
(13) Lansbury, P. T.; Lashuel, H. A. A Century-Old Debate on Protein Aggregation and Neurodegeneration Enters the Clinic. *Nature* **2006**, *443*, 774−779.
(14) Marotta, N. P.; Lin, Y. H.; Lewis, Y. E.; Ambroso, M. R.; Zaro, B. W.; Roth, M. T.; Arnold, D. B.; Langen, R.; Pratt, M. R. O-GlcNAc Modification Blocks the Aggregation and Toxicity of the Protein α-Synuclein Associated with Parkinson's Disease. *Nat. Chem.* **2015**, *7*, 913−920.
(15) Mostaert, A. S.; Higgins, M. J.; Fukuma, T.; Rindi, F.; Jarvis, S. P. Nanoscale Mechanical Characterisation of Amyloid Fibrils Discovered in a Natural Adhesive. *J. Biol. Phys.* **2007**, *32*, 393−401.
(16) Chapman, M. R.; Robinson, L. S.; Pinkner, J. S.; Roth, R.; Heuser, J.; Hammar, M.; Normark, S.; Hultgren, S. J. Role of Escherichia Coli Curli Operons in Directing Amyloid Fiber Formation. *Science* **2002**, *295*, 851−855.
(17) Fowler, D. M.; Koulov, A. V.; Alory-Jost, C.; Marks, M. S.; Balch, W. E.; Kelly, J. W. Functional Amyloid Formation within Mammalian Tissue. *PLoS Biol.* **2005**, *4*, e6.
(18) Knowles, T. P. J.; Mezzenga, R. Amyloid Fibrils as Building Blocks for Natural and Artificial Functional Materials. *Adv. Mater.* **2016**, *28*, 6546−6561.
(19) Jutz, G.; Van Rijn, P.; Santos Miranda, B.; Böker, A. Ferritin: A Versatile Building Block for Bionanotechnology. *Chem. Rev.* **2015**, *115*, 1653−1701.
(20) Reches, M.; Gazit, E. Casting Metal Nanowires Within Discrete Self-Assembled Peptide Nanotubes. *Science* **2003**, *300*, 625−627.
(21) Fan, K.; Cao, C.; Pan, Y.; Lu, D.; Yang, D.; Feng, J.; Song, L.; Liang, M.; Yan, X. Magnetoferritin Nanoparticles for Targeting and Visualizing Tumour Tissues. *Nat. Nanotechnol.* **2012**, *7*, 459−464.
(22) Adamcik, J.; Mezzenga, R. The Amyloid Polymorphism in the Protein Folding and Aggregation Energy Landscape. *Angew. Chem., Int. Ed.* **2018**, *57*, 8370−8382.
(23) Kurouski, D.; Lombardi, R. A.; Dukor, R. K.; Lednev, I. K.; Nafie, L. A. Direct Observation and PH Control of Reversed Supramolecular Chirality in Insulin Fibrils by Vibrational Circular Dichroism. *Chem. Commun.* **2010**, *46*, 7154−7156.
(24) Dzwolak, W.; Loksztejn, A.; Galinska-Rakoczy, A.; Adachi, R.; Goto, Y.; Rupnicki, L. Conformational Indeterminism in Protein Misfolding: Chiral Amplification on Amyloidogenic Pathway of Insulin. *J. Am. Chem. Soc.* **2007**, *129*, 7517−7522.
(25) Petkova, A. T.; Leapman, R. D.; Guo, Z.; Yau, W. M.; Mattson, M. P.; Tycko, R. Self-Propagating, Molecular-Level Polymorphism in Alzheimer's beta-amyloid Fibrils. *Science* **2005**, *307*, 262−265.
(26) Rubin, N.; Perugia, E.; Goldschmidt, M.; Fridkin, M.; Addadi, L. Chirality of Amyloid Suprastructures. *J. Am. Chem. Soc.* **2008**, *130*, 4602−4603.
(27) Seilheimer, B.; Bohrmann, B.; Bondolfi, L.; Müller, F.; Stüber, D.; Döbeli, H. The Toxicity of the Alzheimer's Beta-Amyloid Peptide Correlates with a Distinct Fiber Morphology. *J. Struct. Biol.* **1997**, *119*, 59−71.
(28) Fändrich, M.; Fletcher, M. a.; Dobson, C. M. Amyloid Fibrils from Muscle Myoglobin. *Nature* **2001**, *410*, 165−166.
(29) Jurado, R.; Castello, F.; Bondia, P.; Casado, S.; Flors, C.; Cuesta, R.; Domínguez-Vera, J. M.; Orte, A.; Gálvez, N. Apoferritin Fibers: A New Template for 1D Fluorescent Hybrid Nanostructures. *Nanoscale* **2016**, *8*, 9648−9656.
(30) Adamcik, J.; Jung, J.-M.; Flakowski, J.; De Los Rios, P.; Dietler, G.; Mezzenga, R. Understanding Amyloid Aggregation by Statistical Analysis of Atomic Force Microscopy Images. *Nat. Nanotechnol.* **2010**, *5*, 423−428.
(31) Usov, I.; Adamcik, J.; Mezzenga, R. Polymorphism Complexity and Handedness Inversion in Serum Albumin Amyloid Fibrils. *ACS Nano* **2013**, *7*, 10465−10474.
(32) Uesaka, A.; Ueda, M.; Makino, A.; Imai, T.; Sugiyama, J.; Kimura, S. Morphology Control between Twisted Ribbon, Helical Ribbon, and Nanotube Self-Assemblies with His-Containing Helical Peptides in Response to PH Change. *Langmuir* **2014**, *30*, 1022−1028.
(33) Rubin, N.; Perugia, E.; Wolf, S. G.; Klein, E.; Fridkin, M.; Addadi, L. Relation between Serum Amyloid A Truncated Peptides and Their Suprastructure Chirality. *J. Am. Chem. Soc.* **2010**, *132*, 4242−4248.
(34) Usov, I.; Mezzenga, R. FiberApp: An Open-Source Software for Tracking and Analyzing Polymers, Filaments, Biomacromolecules, and Fibrous Objects. *Macromolecules* **2015**, *48*, 1269−1280.
(35) Adamcik, J.; Lara, C.; Usov, I.; Jeong, J. S.; Ruggeri, F. S.; Dietler, G.; Lashuel, H. A.; Hamley, I. W.; Mezzenga, R. Measurement of Intrinsic Properties of Amyloid Fibrils by the Peak Force QNM Method. *Nanoscale* **2012**, *4*, 4426−4429.
(36) Midgley, P. A.; Dunin-Borkowski, R. E. Electron Tomography and Holography in Materials Science. *Nat. Mater.* **2009**, *8*, 271−280.
(37) Kollmer, M.; Meinhardt, K.; Haupt, C.; Liberta, F.; Wulff, M.; Linder, J.; Handl, L.; Heinrich, L.; Loos, C.; Schmidt, M.; et al. Electron Tomography Reveals the Fibril Structure and Lipid Interactions in Amyloid Deposits. *Proc. Natl. Acad. Sci. U. S. A.* **2016**, *113*, 5604−5609.
(38) Han, S.; Kollmer, M.; Markx, D.; Claus, S.; Walther, P.; Fändrich, M. Amyloid Plaque Structure and Cell Surface Interactions of β-Amyloid Fibrils Revealed by Electron Tomography. *Sci. Rep.* **2017**, *7*, 43577.
(39) Vázquez-Fernández, E.; Vos, M. R.; Afanasyev, P.; Cebey, L.; Sevillano, A. M.; Vidal, E.; Rosa, I.; Renault, L.; Ramos, A.; Peters, P. J.; et al. The Structural Architecture of an Infectious Mammalian Prion Using Electron Cryomicroscopy. *PLoS Pathog.* **2016**, *12*, e1005835.
(40) Lopez-Haro, M.; Guétaz, L.; Printemps, T.; Morin, A.; Escribano, S.; Jouneau, P.-H.; Bayle-Guillemaud, P.; Chandezon, F.; Gebel, G. Three-Dimensional Analysis of Nafion Layers in Fuel Cell Electrodes. *Nat. Commun.* **2014**, *5*, 5229.
(41) Rueda-Fonseca, P.; Robin, E.; Bellet-Amalric, E.; Lopez-Haro, M.; Den Hertog, M.; Genuist, Y.; André, R.; Artioli, A.; Tatarenko, S.; Ferrand, D.; et al. Quantitative Reconstructions of 3D Chemical Nanostructures in Nanowires. *Nano Lett.* **2016**, *16*, 1637−1642.
(42) Paravastu, A. K.; Leapman, R. D.; Yau, W.; Tycko, R. Molecular Structural Basis for Polymorphism in Alzheimer's beta-Amyloid Fibrils. *Proc. Natl. Acad. Sci. U. S. A.* **2008**, *105*, 18349−18354.
(43) Onogi, S.; Shigemitsu, H.; Yoshii, T.; Tanida, T.; Ikeda, M.; Kubota, R.; Hamachi, I. In Situ Real-Time Imaging of Self-Sorted Supramolecular Nanofibres. *Nat. Chem.* **2016**, *8*, 743−752.
(44) Aliprandi, A.; Mauro, M.; De Cola, L. Controlling and Imaging Biomimetic Self-Assembly. *Nat. Chem.* **2016**, *8*, 10−15.
(45) Bondia, P.; Jurado, R.; Casado, S.; Domínguez-Vera, J. M.; Gálvez, N.; Flors, C. Hybrid Nanoscopy of Hybrid Nanomaterials. *Small* **2017**, *13*, 1−7.
(46) Castello, F.; Paredes, J. M.; Ruedas-Rama, M. J.; Martin, M.; Roldan, M.; Casares, S.; Orte, A. Two-Step Amyloid Aggregation: Sequential Lag Phase Intermediates. *Sci. Rep.* **2017**, *7*, 40065.
(47) Schindelin, J.; Arganda-Carreras, I.; Frise, E.; Kaynig, V.; Longair, M.; Pietzsch, T.; Preibisch, S.; Rueden, C.; Saalfeld, S.; Schmid, B.; et al. Fiji: An Open-Source Platform for Biological-Image Analysis. *Nat. Methods* **2012**, *9*, 676−682.

DOI: 10.1021/jacs.8b11418
J. Am. Chem. Soc. 2019, 141, 1606−1613